Research Article

Hanjun Gao, Minghui Lin, Jing Guo, Liang Yang, Qiong Wu*, Ziliang Ran, and Nianpu Xue

A simulation modeling methodology considering random multiple shots for shot peening process

https://doi.org/10.1515/rams-2022-0304
received June 02, 2022; accepted January 20, 2023

Abstract: Shot peening (SP) process is a typical surface strengthening process for metal and metal matrix composites, which can significantly improve the fatigue life and strength. The traditional SP simulation model falls short as it only takes into account one or a few shots, proving insufficient for accurately simulating the entire impact process involving hundreds of shots. In this study, a random multiple shots simulation modeling methodology with hundreds of random shots is proposed to simulate the impact process of SP. In order to reduce the simulation error, the random function Rand of MATLAB is used to generate the shot distributions many times, and the shot distribution closest to the average number is selected and the three-dimension parametric explicit dynamics numerical simulation model is built using ABAQUS software. Orthogonal experiments are carried out to investigate the influences of shot diameter, incident impact velocity, and angle on the residual stress distribution, roughness, and specimen deformation. Results showed that the average relative errors of maximum residual compressive stress, roughness, and deformation of specimen between simulation model and experimental value are 30.99, 16.14, and 16.73%, respectively. The primary factors affecting residual stress and deformation is shot diameter, and the main factor affecting roughness is impact velocity.

Keywords: shot peening, random multiple, residual stress, roughness, deformation

1 Introduction

The mechanical strength, dimensional accuracy, and fatigue life of the material largely depend on the internal stress state of the material [1,2]. For most materials, the ability to bear compressive stress is stronger, and the ability to bear tensile stress is weaker [3]. Compressive stress often has a positive effect on the structural strength, while tensile stress has a negative effect [4]. Therefore, the stress state of materials has been widely concerned by scholars, among which the stress–strain constitutive relationship and the effect of stress state on the mechanical properties and microstructure are the main concerns [5].

Sun *et al.* [6] found that the size and the number of self-formed Ag particles on the Ag–Mo (Zr) alloy film are closely related to the different thermal stress evolution behaviors of the alloy films on different substrates during annealing. Ni *et al.* [7] compared two series of gradient nanostructured nickel with symmetric structures and the homogeneous counterparts with three levels of grain size based on macro-statistical data to investigate the effect of stress states on the deformation behavior. Li *et al.* [8] summarized the various particle reinforced composite and stress buffer metal interlayer added composite for brazing C/C composite. Zhao and Gu [9] used 3D optical measuring digital image correlation (DIC) to systematically measure the full strain field and actual flow stress in the necking region of ultrafine-grained aluminum alloy. Gao *et al.* [10] used four typical particle modeling methods to establish a geometric model, and found that the micro

* **Corresponding author: Qiong Wu,** State Key Laboratory of Virtual Reality Technology and Systems, School of Mechanical Engineering and Automation, Beihang University, Beijing, 100191, China; Mechanical Design and Manufacturing Simulation Analysis Laboratory, Jingdezhen Research Institute, Beihang University, Jingdezhen, 333000, China, e-mail: wuqiong@buaa.edu.cn, tel: +86-010-82317756
Hanjun Gao: State Key Laboratory of Virtual Reality Technology and Systems, School of Mechanical Engineering and Automation, Beihang University, Beijing, 100191, China; Mechanical Design and Manufacturing Simulation Analysis Laboratory, Jingdezhen Research Institute, Beihang University, Jingdezhen, 333000, China
Minghui Lin, Ziliang Ran, Nianpu Xue: State Key Laboratory of Virtual Reality Technology and Systems, School of Mechanical Engineering and Automation, Beihang University, Beijing, 100191, China
Jing Guo: School of Mechanical Engineering, Beijing Institute of Technology, 100081, Beijing, China; Research and Development Department, Key Laboratory of Vehicle Transmission, China North Vehicle Research Institute, Beijing, 100072, China
Liang Yang: Research and Development Department, Shanghai Space Propulsion Technology Research Institute, Shanghai, 201101, China

stress distribution of matrix and particles conforms to the normal distribution law, while the interface stress does not conform to the normal distribution law.

The interfacial shear strength of the carbon nanotube-polyimide nanocomposites was calculated using molecular dynamics simulations by Jiang *et al.* [11], and the results showed that increasing the number of walls is a critical factor for enhancing the interfacial stress transfer during tension. Wang *et al.* [12] established a model of cell density vs stress through a specific normalization method for 3D culturing of MC3T3-E1 cells, and analyzed the detailed influence of stress on cell proliferation.

Zhang *et al.* [13] believed that the stress response was found to be different in the regions with different grain sizes of gradient nano-grained copper, and it was attributed to different dislocation activities due to the dislocation–grain boundary synergies. Akbar and Mehmood [14] summarized that a long-term exposure of DC composite insulators to various outdoor environmental and electrical stresses cause aging of these insulators.

Shot peening (SP) is a mature surface strengthening technology, which can evidently improve the surface strength by inducing residual compressive stress in the surface [15,16]. SP strength is usually calibrated by the bending distortion of Almen test specimen. The larger the bending distortion of test specimen is, the greater the stress generated by SP is [17]. Therefore, in principle, the residual stress induced by SP will also cause a certain amount of deformation of the specimen [18]. The influence of SP process parameters on the surface residual stress layer and fatigue life of parts is the main problem in the relative field, and the control of the SP deformation is also a concern [19]. The modified and improved processes, such as laser shot peening (LSP) and ultrasonic impact peening, are also widely focused by researchers.

Mahmoudi *et al.* [20] established numerical model to study the redistribution of residual stresses induced by SP. An analytical approach is proposed by Sherafatnia *et al.* [21] to determine the residual stresses induced by SP with considering conditions of previous treatments. Marini *et al.* [22] proposed a synergistic approach based on discrete element method and finite element method (FEM) to simulate SP process. Ghasemi *et al.* [23] proposed a novel FE-based model to predict the effect of coverage on the surface state, and the effects of Rayleigh damping, mesh size, and target dimensions on residual stress profile were investigated. Atig *et al.* [24] used a probabilistic methodology to evaluate the residual stress and Almen intensity in the SP process.

Tan *et al.* [25] demonstrated the compressive residual stress profile induced by milling process using an exponential decay function, and they proposed a sinusoidal decay function to demonstrate the residual stress generated by SP. Zhu *et al.* [26] found that the depth of the projectile indentation increased and the surface roughness became larger with increasing SP intensity by treating the 1.5 wt% CNT/6061 composite with five different intensities. The compressive residual stress field was introduced after SP. Chen *et al.* [27] showed that multiple SP is effective in generating deep layer of high compressive residual stress with moderate work hardening. The maximum compressive residual stress reaches −1070.5 and −910.5 MPa after triple SP. Trško *et al.* [28] observed an unexpected significant fatigue strength improvement in the ultra-high cycle region after SSP surface treatment. Vázquez *et al.* [29] presented that SP can improve the fretting fatigue life of Al 7075-T651 by generating compressive residual stresses. Wu *et al.* [30] investigated the residual stress distribution of SiCp/2024Al under the influence of SP radius, speed, and angle.

Bagherifard *et al.* [31] concluded that severe SP has better fatigue strength improvement than conventional SP, but the surface roughness is also high because of the energy impacts. Bagherifard *et al.* [32] also demonstrated that severe SP induced near the surface grain refinement to nano and sub-micron range transformed the austenite phase into strain-induced α′-martensite in a layered deformation band structure. Hassani-Gangaraj *et al.* [33] used air blast SP over a wide range of coverage, including conventional to severe SP, to generate nanostructured surface layers on high strength low alloy steel. Almangour and Yang [34] induced grain refinements through an SP process generating severe plastic deformation at the outer surface to increase the mechanical properties of 3D print 17-4 stainless steel.

Moreover, Sun *et al.* [35] presented that residual stresses are changed from tensile to compressive state after LSP treatment, and yield strength was remarkably increased by 72%. Sorsa *et al.* [36] found that when SP intensity is over 0.5 mmA, the intensity dominates the SP coverage density parameter. Gujba and Medraj *et al.* [37] found that the depth of the compressive residual stress layer induced by LSP is 4–5 times as that induced by conventional SP, but SP is more effective to the coatings than LSP.

Although many studies have been conducted to investigate the SP process, existing calculation models cannot practically present the randomness and coverage of shots, which will greatly limit the calculation accuracy of the prediction model. In this study, a random multiple shots simulation modeling methodology with random hundreds of shots is proposed to simulate the impact process of SP, and corresponding experiments are conducted to verify the accuracy of the proposed model. Finally, the effects

of SP speed, incidence angle, and shot diameter on the residual stress, roughness, and deformation are investigated based on the experiment and simulation results.

2 Modeling, simulation, and experiments

2.1 Orthogonal design of process parameters

SP is a highly random, discrete, and nonlinear process. The residual compressive stress of the surface induced by SP can effectively restrain the nucleation and propagation of fatigue cracks. However, the resulting increase in surface roughness and deformation has negative effects on the fatigue life and the dimensional stability. Therefore, residual compressive stress, roughness, and deformation should be taken as the evaluation indexes at the same time.

In order to investigate the influences of SP parameters on residual stress, roughness, and deformation of Ti–6Al–4V, SP process parameters, including shot diameter, impact velocity, and impact angle (Table 1), are determined by orthogonal table, and the range analysis is conducted to find the optimum combination of SP process parameters. As shown in Table 2, three factors are all three levels, which cover the common process parameters, of which the shot diameter is 0.2, 0.3, and 0.5 mm, the impact angle is 90°, 60°, and 30°, and the impact velocity is 60, 80, and 100 $m{\cdot}s^{-1}$.

2.2 Modeling and simulation

Table 3 presents the chemical composition of Ti–6Al–4V, and Table 4 presents the basic material parameters of Ti–6Al–4V and cast steel shot. The material generates elastic-plastic deformation during SP, and its yield limit will change at different strain rates. The constitutive equation is determined to establish a more accurate finite element model. Johnson–Cook (J–C) constitutive equation taking into account the effects of strain hardening, strain rate hardening, and thermal softening comprehensively is used in this study. J–C constitutive equation of Ti–6Al–4V used in this study is expressed as follows [38]:

$$\sigma_f = [A + B\varepsilon_{eff}^{n}][1 + C \ln \dot{\varepsilon}^{*}][1 - T^{*^{m}}], \quad (1)$$

where σ_f is von Mises flow stress, ε_{eff} is the equivalent plastic strain, $\dot{\varepsilon}^{*}$ is the dimensionless equivalent plastic strain rate, T^{*} is the uniform temperature, and A, B, n, C are undetermined parameters related to materials, $\dot{\varepsilon}^{*} = \dot{\varepsilon}/\dot{\varepsilon}_0$, $\dot{\varepsilon}_0$ is the reference strain rate, $T^{*} = (T - T_r)/(T_m - T_r)$, T_r is the reference temperature, and T_m is the melting point of the material. The parameters of the model are shown in Table 5 [39].

In SP process, the position of the shot is random on the shot path. The randomly distributed shot at high speed constitutes the flow of shot, which evidently affects the surface quality. Therefore, a random multiple impingement SP model is proposed in this study. The coordinate points of the ball center in the space above the target are generated by using the random function "Rand" of MATLAB. The impact area of the shot is within 2.5 times of the diameter of the shot centered on the target. To ensure that no overlap occurs at any two shots in space, the distance between the coordinate points of the spherical center of all generated shots is judged to determine whether the distance is larger than the diameter of the shots.

SP coverage ratio is the ratio of the shot crater area to the surface area of the specimen. Since it is difficult to achieve 100% coverage in practice, it is considered as full coverage when the coverage rate exceeds 98%. In simulation model, the coverage ratio corresponds to the shot number in a certain area, and it increases with the shot number. In addition, the coverage is related to the crater area of the shot, so it is necessary to calculate the crater area of a single shot before calculating the coverage ratio. The crater projection of a single shot is approximately a circle and the crater area can be obtained according to the crater diameter. The displacement of target impact

Table 1: Factors and factor levels

Level	Factor		
	A **– shot diameter (mm)**	***B*** **– impact velocity ($m{\cdot}s^{-1}$)**	***C*** **– impact angle (°)**
1	0.2	60	90
2	0.3	80	60
3	0.5	100	30

Table 2: SP orthogonal table

Case	Shot diameter (mm)	Impact velocity ($m{\cdot}s^{-1}$)	Impact angle (°)
1	0.2	60	90
2	0.2	80	60
3	0.2	100	30
4	0.3	60	60
5	0.3	80	30
6	0.3	100	90
7	0.5	60	30
8	0.5	80	90
9	0.5	100	60

Table 3: Chemical composition of Ti–6Al–4V

Element composition	Al	V	Fe	O	C	N	H	Ti
Percentage	5.5–6.75	3.5–4.5	<0.3	<0.2	<0.08	<0.05	0.015	Balance

Table 4: Basic material parameters of target and shot

Material parameters	Ti–6Al–4V	Cast steel
Density (t·mm^{-3})	4.42×10^{-9}	7.80×10^{-9}
Modulus of elasticity (GPa)	110	200
Elastic Poisson's ratio	0.342	0.3
Yield strength (GPa)	1.100	—
Tensile strength (GPa)	1.170	—

Table 5: J–C constitutive equation parameters of Ti–6Al–4V

A (MPa)	B (MPa)	n	m	T_m (K)	T_r (K)	C	$\dot{\varepsilon}_0$
1,098	1,092	0.93	1.1	1,878	298	0.014	1

area along the depth direction can be obtained using single impingement SP model under different process parameters. Then, the crater displacement curves of shot are extracted, and the two-point distance with zero displacement along the depth direction is taken as the crater diameter (Figure 1).

After obtaining the crater diameter impacted by single shot, the impact area of shot is divided into 100 parts in X direction and Y direction to obtain the coverage ratio, and each direction contains 101 nodes, generating 101 × 101 nodes in total. Spherical center coordinate of each shot is generated randomly in the impact area, and the distance from each node to all shot centers is calculated. If the distance from one node to all shot centers is greater than the crater radius, the node is in the unshot-peened area [40]. The node number in the shot-peened area is defined as M, then the coverage ratio C is as follows:

$$C = \frac{M}{101 \times 101} \times 100\%. \tag{2}$$

If C is less than 98%, increase in the shot number is greater than or equal to 98%. At this time, the shot numbers and the spatial coordinates are recorded (Figure 2), wheremin($D_{1,i-j}$) is the minimum distance between the i-th shot center and j-th shot center, R_{shot} is the shot radius, min($D_{2,k-i}$) is the minimum distance between the k-th node and the shot center of all i shots.

Moreover, the shot coordinates in the simulation model are randomly generated, so the single calculation result of coverage ratio has certain randomness with the same parameter. That is, under the same parameters, the shot number obtained by two calculations is not necessarily the same, and the big difference of the shot number will greatly affect the accuracy of simulation results. In fact, the number of shots is very large. In order to reduce the random error of simulation results, the shot number in the area with 2.5 times shot diameter is counted, and random coordinates satisfying 98% coverage ratio are generated for dozens of times. Then, the shot coordinates closest to the average number are selected for FE modeling.

Taking Case 9 as an example, in the area of 2.5 times the shot sectional area (1.25 mm × 1.25 mm), the shot number distribution is shown in Figure 3, and the

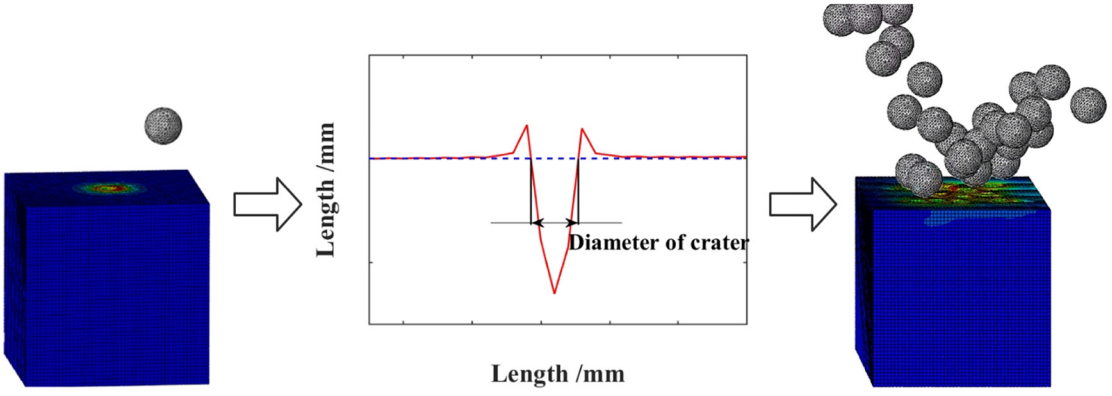

Figure 1: Diameter of crater.

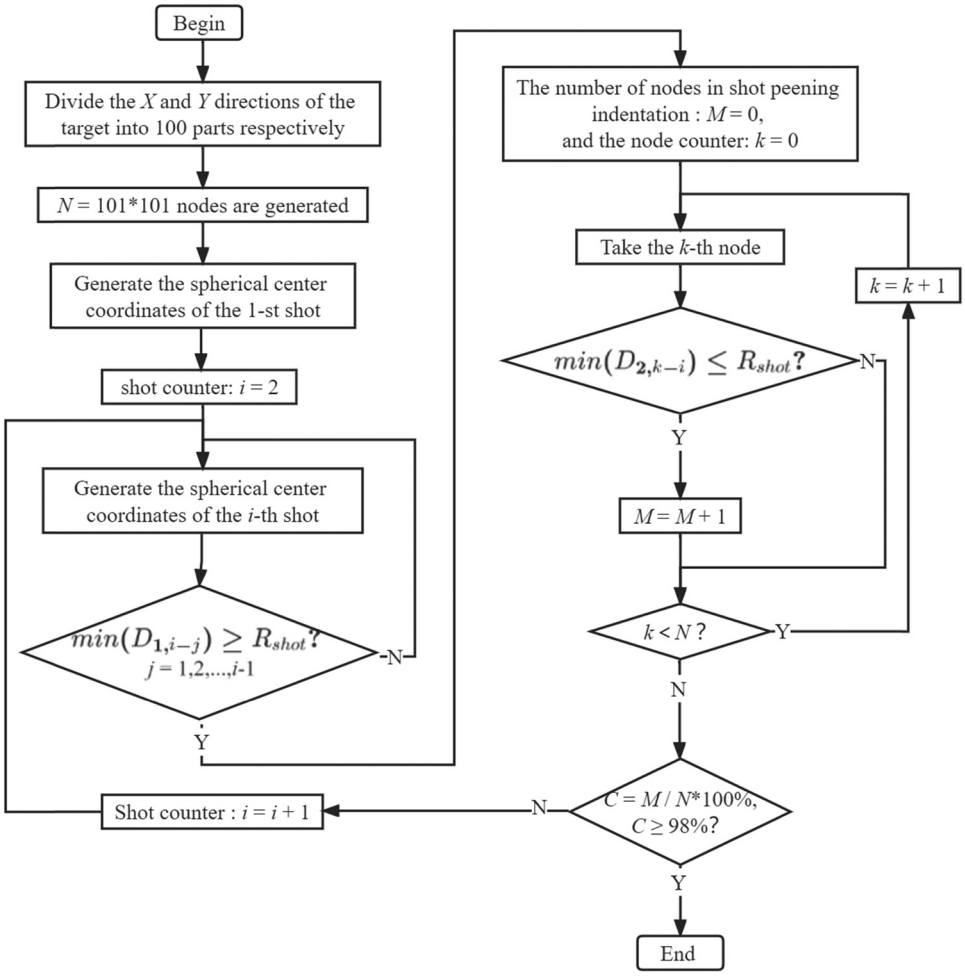

Figure 2: The flow chart of the coverage calculation.

average value of shot number satisfying 98% coverage is 193.57, and the other cases are shown in Figure A1 in the appendix. Each case in Table 2 has been calculated for 2,000 times, respectively, and the average number of each case is shown in Figure 4. It shows that the average number of shots required in the studied area increases with the diameter ratio of shot crater. The shot numbers required to satisfy 98% coverage and the diameter ratios of shot crater obtained under different process plans are linearly fitted by least square method (Eq. (3)).

$$N = 217.3 \cdot \frac{D_1}{D_2} - 313.5, \tag{3}$$

where N is the number of shots, D_1 is the diameter of the shot, and D_2 is the crater diameter.

However, even if the shot numbers are the same, the calculation results also have some randomness due to the different shot coordinates. That is, the results of two simulations are different under the same parameters. In order to further reduce the random error of simulation results, four groups of shot coordinates closest to the average number are applied for modeling.

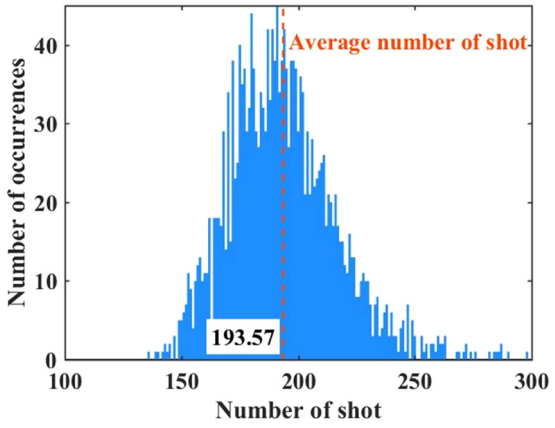

Figure 3: 2,000 times calculation of shot number distribution in Case 9 (0.5 mm/100 m·s^{-1}/60°).

The residual stress and node coordinates of target in unconstrained and stable state after SP are extracted in simulation model to investigate the influence of SP process parameters on the surface residual stress and roughness. Then, the reference plane is fitted by node coordinates to calculate the roughness-related parameters.

In addition, the specimens are designed to investigate the influence of SP process parameters on deformation. Figure 5 shows the shape, size, and tolerance of specimen and specify that the long side is in the X direction and the short side is in the Y direction. Because the specimens are symmetrical structure, 1/4 of the geometric model and symmetrical constraints are used for modeling. The residual stresses in the X and Y directions after SP are obtained according to the FE model.

2.3 Experiments

Nine specimens, numbered Case 1–9, are machined according to Figure 5. The specimen is de-stress annealed after machining to eliminate the influence of residual stress caused by machining induced residual stress. The heat treatment process are as follows: heating slowly from room temperature to 600°C, holding for 2 h, cooling with the furnace, and conducting SP according to 1–9 process parameters in Table 2.

In experiments, the conversion relationship between the shot velocity $V_s$and shot pressure P_s, shot flow rate m and shot diameter D_s is determined as follows [40]:

$$V_s = 1.55\left(\frac{16.35P_s}{1.53m + P_s} + \frac{29.5P_s}{0.598D_s + P_s} + 4.83P_s\right). \quad (4)$$

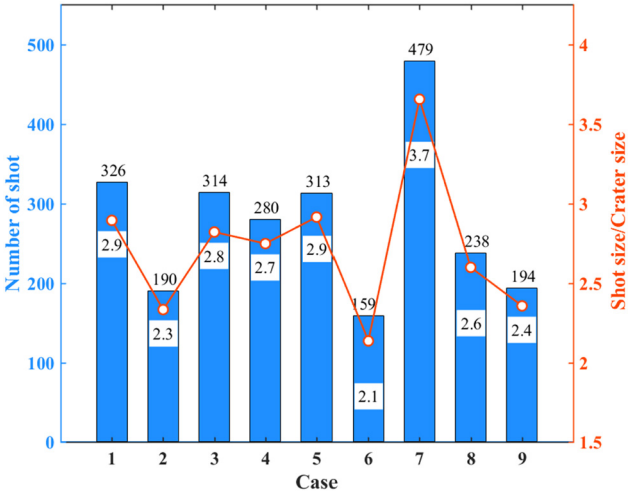

Figure 4: Average number of shots and the diameter ratio of shot to crater for 2,000 times calculation.

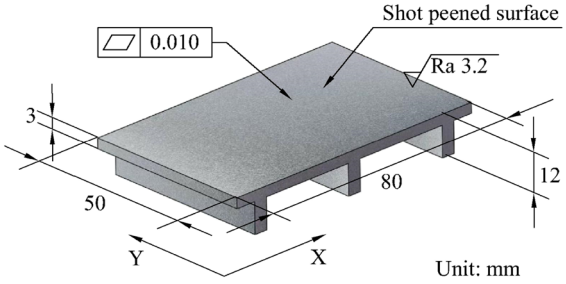

Figure 5: Shape, size, and tolerance of the specimen.

The SP experiment equipment used is the TC170S69F rotary frequency conversion shot peening machine produced by Beijing Yiyang Yingzhen Testing Technology Co. SP parameters in the experiments are shown in Table A1, and the pressure fluctuation of the equipment is ±0.2 bar.

The diameter of the spray gun muzzle is about 36 mm. As shown in Figure A2, the two sides in the length direction of specimens are fixed with clamps during SP, and the gun moves along the length direction along the specimen surface. The shot with diameters of 0.2, 0.3, and 0.5 mm used in the experiment are S70, S110, and S170 (ISO11124-3), respectively.

The residual stress in length and width directions on the center point of shot-peened surface is measured using Prism Electronic Speckle Interference Bore Residual Stress Meter from Stresstech Group (Figure A3a), Finland. The measurements are token at intervals of 0.025 mm and the deepest point.

Surface roughness is measured by CCI-MP-HS non-contact white light interference profilometer (Figure A3b) manufactured by Amertec. The specimen can be moved through the base to measure different positions, and the regional roughness results of specimen surface can be obtained. 3D surface profiles at three points of each specimen are measured, and the positions of the measuring points are shown in Figure 6.

After stress relief annealing, the specimen is placed on a machine tool workbench with a pressure gauge and a digital display meter (Figure A3c). The distance between the pressure gauge probe and the workbench can be read by the digital display meter with an accuracy of 0.001 mm.

3 Results and discussion

3.1 Residual stress

The residual stresses in X (length) and Y (width) directions of the specimens in unconstrained state after SP are

extracted from four groups of simulation models under each process parameter, and the average stresses of the four groups of models under the same process parameters are obtained. Then, the obtained data are cubic spline interpolated.

Figure 7 shows the simulation and experiment results of residual stress in X and Y directions. It shows that the trend and magnitude of simulation results are consistent with that of the experiment results. Residual stress presents obvious "hook" distribution. Compressive residual stress increases with the depth and reaches the maximum value at a certain depth, then decreases with the depth and finally converts into tensile stress.

Compressive residual stresses can offset the tensile stresses caused by partial working loads, which are generally considered to be the main reason for increasing the fatigue life of materials. In addition, the consistency of the measured residual stresses is not as good as that of the simulation results due to the systematic error of equipment and random error.

Table A2 shows the maximum compressive residual stress of Cases 1–9 obtained by simulations and experiments. It shows that the simulated maximum compressive residual stress is around −800 MPa. Simulation results have some errors compared with the experimental data. The average relative error of the maximum compressive residual stress is 30.99%. The simulated residual compressive stress is larger than that in the experiment, because the shot is set as a rigid body in the simulation to improve the calculation efficiency, which results in the deeper impact depth of the shot.

The average of residual stresses in X and Y directions at the same depth of 9 specimens are obtained based on the experimental results, and cubic spline interpolated interpolations are performed to obtain the average residual stress in X and Y directions at every 0.001 mm depths. Because the units of acquired target data values are not uniform, it is very difficult to directly superimpose the four index data to evaluate the SP effect achieved by each set of parameters. Thus, in order to evaluate effectively, comprehensive scoring method is adopted as follows:

$$\text{Individual score} = \frac{\text{Individual index value}}{\text{Maximum value of Individual index}} \times 100, \tag{5}$$

$$\begin{aligned}\text{Comprehensive score} = {} & b1 \times \text{Individual score 1} \\ & + b2 \times \text{Individual score 2} \\ & + b3 \times \text{Individual score 3} \\ & + b4 \times \text{Individual score 4},\end{aligned} \tag{6}$$

where Individual scores 1, 2, 3, and 4 refer to the depth of residual compressive stress layer, surface residual compressive stress value, maximum residual stress value depth, and maximum residual compressive stress value, respectively. $b1$, $b2$, $b3$, and $b4$, respectively, refer to the weight of the four individual scores in the comprehensive score.

The weighting coefficient of each individual score is given according to the importance of target in SP effect, and weighted sum is made to convert multi-objective evaluation index into comprehensive single-objective

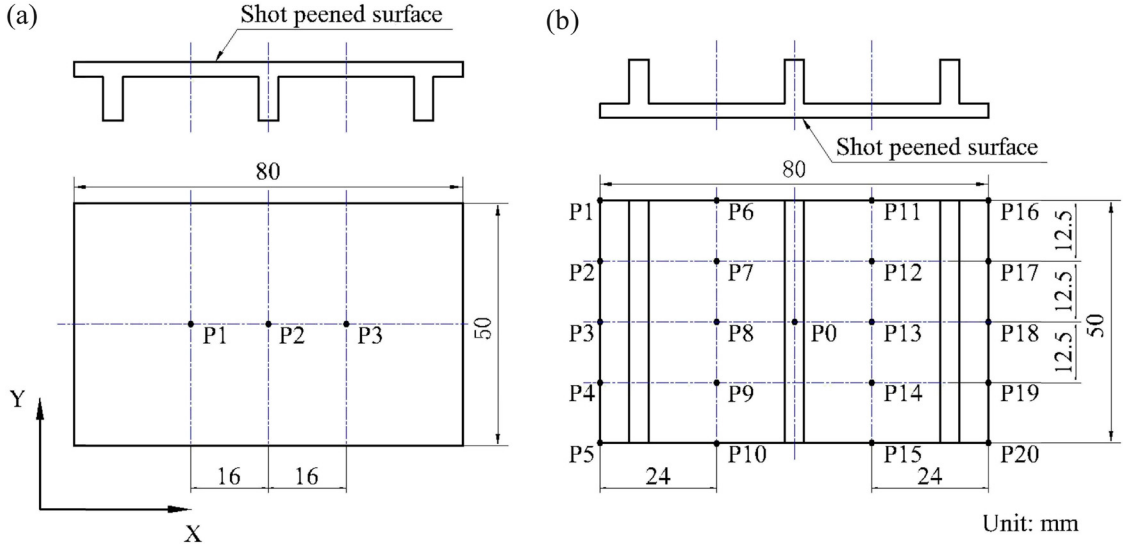

Figure 6: Experimental test point. (a) Roughness test point and (b) deformation test point.

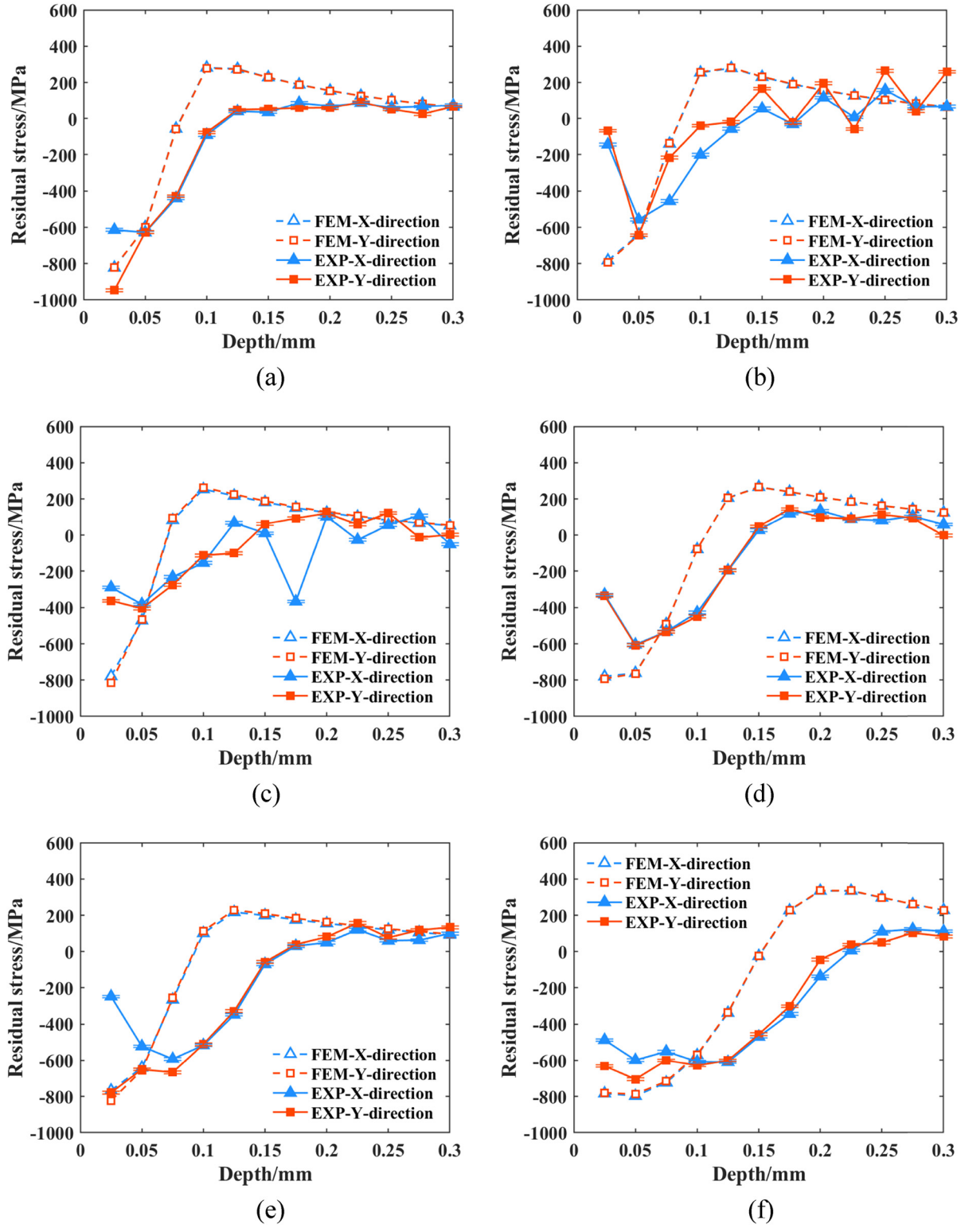

Figure 7: The comparison of the residual stress between the simulation and the experimental data. (a) Case 1 (0.2 mm/60 m·s^{-1}/90°). (b) Case 2 (0.2 mm/80 m·s^{-1}/60°). (c) Case 3 (0.2 mm/100 m·s^{-1}/30°). (d) Case 4 (0.3 mm/60 m·s^{-1}/60°). (e) Case 5 (0.3 mm/80 m·s^{-1}/30°). (f) Case 6 (0.3 mm/100 m·s^{-1}/90°). (g) Case 7 (0.5 mm/60 m·s^{-1}/30°). (h) Case 8 (0.5 mm/80 m·s^{-1}/90°). (i) Case 9 (0.5 mm/100 m·s^{-1}/60°).

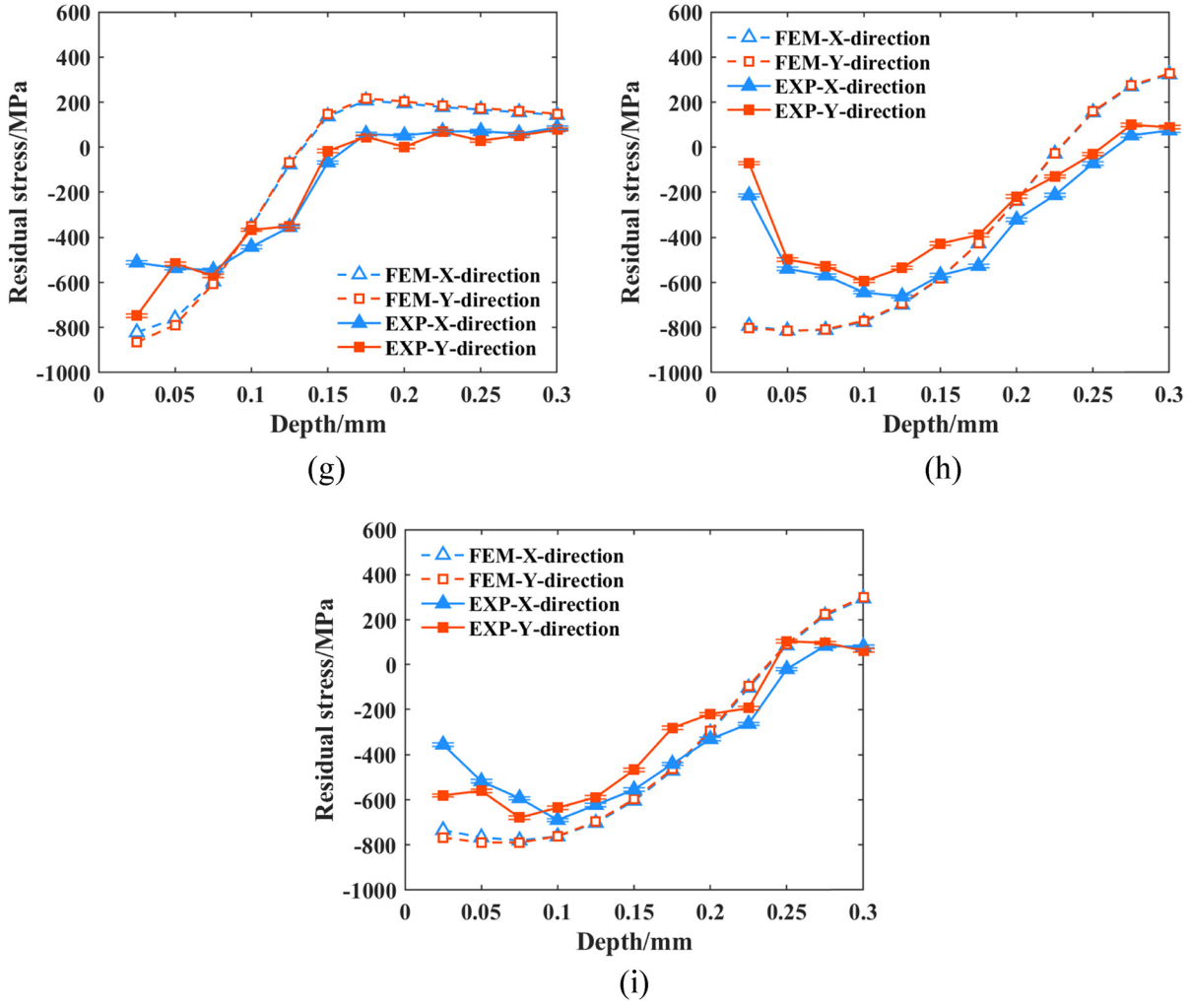

Figure 7: (*Continued*)

evaluation index. The weights for the four individual scores are all 25%, and the comprehensive score of residual stress test results for each parameter is shown in Table 6.

In order to get the relationship between each process parameter and comprehensive index and obtain the best combination of parameters of comprehensive index, the

Table 6: Comprehensive score of residual stress test results

Case	Depth of residual compressive stress (mm)	Surface residual stress (MPa)	Maximum residual compressive stress (MPa)	Depth of maximum residual compressive stress (mm)	Comprehensive score
1	0.111 ± 0.001	−780.58 ± 282.25	−780.58 ± 244.63	0.025 ± 0.021	66.45
2	0.131 ± 0.004	−105.82 ± 42.68	−601.43 ± 92.31	0.049 ± 0.009	46.54
3	0.128 ± 0.014	−325.77 ± 74.63	−408.44 ± 39.04	0.042 ± 0.001	45.50
4	0.145 ± 0.001	−331.59 ± 29.12	−607.42 ± 48.43	0.052 ± 0.000	56.00
5	0.161 ± 0.001	−512.98 ± 394.54	−633.13 ± 102.25	0.070 ± 0.003	68.30
6	0.218 ± 0.009	−559.52 ± 139.33	−660.42 ± 95.23	0.043 ± 0.100	69.98
7	0.155 ± 0.006	−629.86 ± 206.28	−629.86 ± 146.75	0.025 ± 0.058	61.04
8	0.259 ± 0.006	−142.15 ± 84.64	−628.37 ± 10.48	0.109 ± 0.010	74.68
9	0.246 ± 0.010	−468.03 ± 186.72	−664.99 ± 17.74	0.095 ± 0.010	81.82

Table 7: Result of range analysis by residual stress comprehensive scoring

Factor	*A* – shot diameter	*B* – impact velocity	*C* – impact angle
Average of level 1	52.83 ± 11.81	61.16 ± 5.23	70.37 ± 4.13
Average of level 2	64.76 ± 7.63	63.17 ± 14.76	61.45 ± 18.27
Average of level 3	72.51 ± 10.56	65.77 ± 18.52	58.28 ± 11.65
Range	19.68	4.61	12.09
Factor primary → secondary	*ACB*		
Optimal plan		$A_3B_3C_1$	

extreme difference of each factor are obtained using range analysis method (Table 7).

From Table 7, it can be seen that the extreme difference of factor *A* is the largest, and is much larger than the other two factors, which indicates that the level of factor *A* has the greatest influence on the experimental results and it is the most important factor affecting the stress hardening effect of SP. The order of each factor from primary to secondary is: *A* (shot diameter), *C* (impact angle), and *B* (impact velocity). The best process combination for stress strengthening is $A_3B_3C_1$. That is, shot diameter is 0.5 mm, shot speed is 100 m·s^{-1}, and impact angle is 90°.

When the weights of the depth of residual compressive stress layer, surface residual compressive stress value, maximum residual stress value, and maximum residual compressive stress value are 17, 33, 17, and 33%, respectively [41], the range of factor *A* is 14.48, factor *B* is 6.40, and factor *C* is 11.34. And the same conclusion can be got as above: the most important factor affecting the stress hardening effect of SP is factor *A* (shot diameter), followed by factor *C* (impact angle), and finally *B* (impact velocity).

In addition, the influence of ceramic shots on the stress strengthening effect of Ti–6Al–4V is studied through the simulation model. The density of ceramic shots is 3.85 × 10^{-9} t·mm^{-3}, Young's modulus of elasticity is 350 GPa, and elastic Poisson's ratio is 0.26 [42]. In order to compare the calculation results of ceramic shots and cast steel shots, the process parameters corresponding to Cases 4–6 of cast steel shots are selected, that is, Case 4-ceramic (0.3 mm/60 m·s^{-1}/60°), Case 5-ceramic (0.3 mm/80 m·s^{-1}/30°), and Case 6-ceramic (0.3 mm/100 m·s^{-1}/90°). As mentioned above, the crater diameter of a single shot needs to be obtained to calculate the number of shots satisfying 98% coverage. The diameter ratio of shot to crater of Case 4-ceramic, Case 5-ceramic, and Case 6-ceramic is 3.0, 3.8, and 2.7, respectively. And the average value of the required number of shots is 353, 520, and 281, respectively, by MATLAB. Figure A4 shows the ceramic SP and cast steel SP results of residual stress in *X* and *Y* directions.

It can be seen from Figure A4 that the trend of the simulation results of ceramic shot and cast steel shot is the same, and the residual compressive stress reaches the maximum at a certain depth, then gradually decreases with the increase in depth, and finally turns into tensile stress. The maximum compressive stress of ceramic shot and cast steel shot is almost the same with the same process parameters, about −800 MPa, and the maximum tensile stress is almost the same, too. The difference is that the depth of stress layer of ceramic shot is less than that of cast steel shot. This is because the density of ceramic is less than that of steel. The kinetic energy carried by ceramic shot is less than that of cast steel shot with the same process parameters, resulting in smaller crater diameter and smaller depth of stress layer.

3.2 Roughness

Figure 8 shows that the surfaces of Case 1, Case 2, Case 3, Case 4, Case 5, and Case 7 with low SP strength have regular undulating contours caused by machining, and the contour of tool marks can still be observed. But the surfaces of Case 6, Case 8, and Case 9 with high SP strength become chaotic and uneven due to the impact of shot, and tool marks can barely be observed.

S_a is the arithmetic mean used to describe the absolute value of the distance from each point in the measured area to the reference plane height, that is, the arithmetic mean height in the sampling area. S_a is the most commonly used topographic feature parameter in surface three-dimension evaluation, so S_a is used to represent the roughness of shot-peened surfaces. The measured results of S_a for Cases 1–9 are shown in Table A3.

In the simulation model, the shot is set as rigid body, which leads to the large depth of the crater during multiple impacts. As a result, the displacement of the surface nodes obtained in the simulation model is relatively large. On the other hand, machining process generates

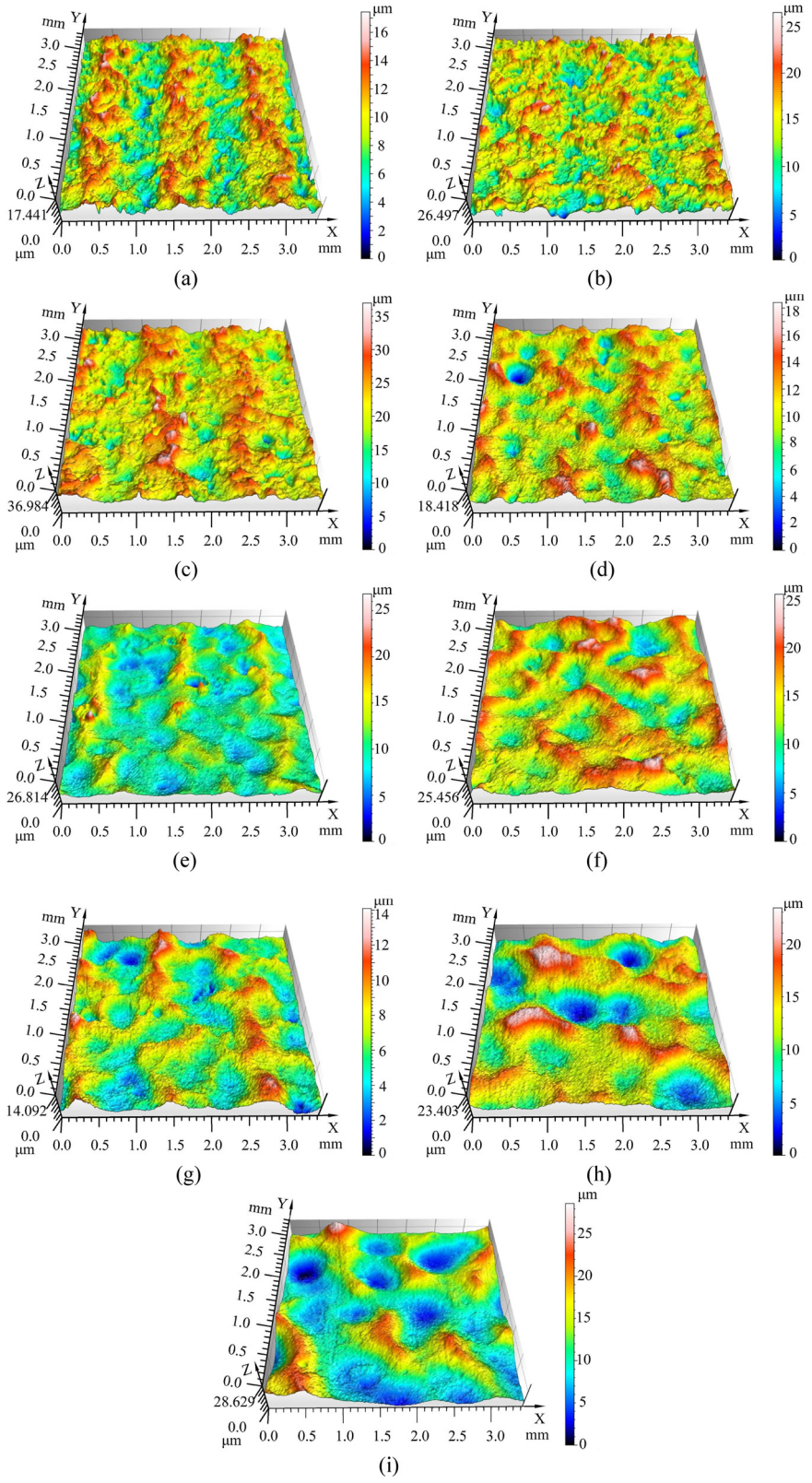

Figure 8: Three-dimension cloud map of the surface contour of Cases 1–9 in *Z* direction. (a) Case 1 (0.2 mm/60 m·s^{-1}/90°). (b) Case 2 (0.2 mm/80 m·s^{-1}/60°). (c) Case 3 (0.2 mm/100 m·s^{-1}/30°). (d) Case 4 (0.3 mm/60 m·s^{-1}/60°). (e) Case 5 (0.3 mm/80 m·s^{-1}/30°). (f) Case 6 (0.3 mm/100 m·s^{-1}/90°). (g) Case 7 (0.5 mm/60 m·s^{-1}/30°). (h) Case 8 (0.5 mm/80 m·s^{-1}/90°). (i) Case 9 (0.5 mm/100 m·s^{-1}/60°).

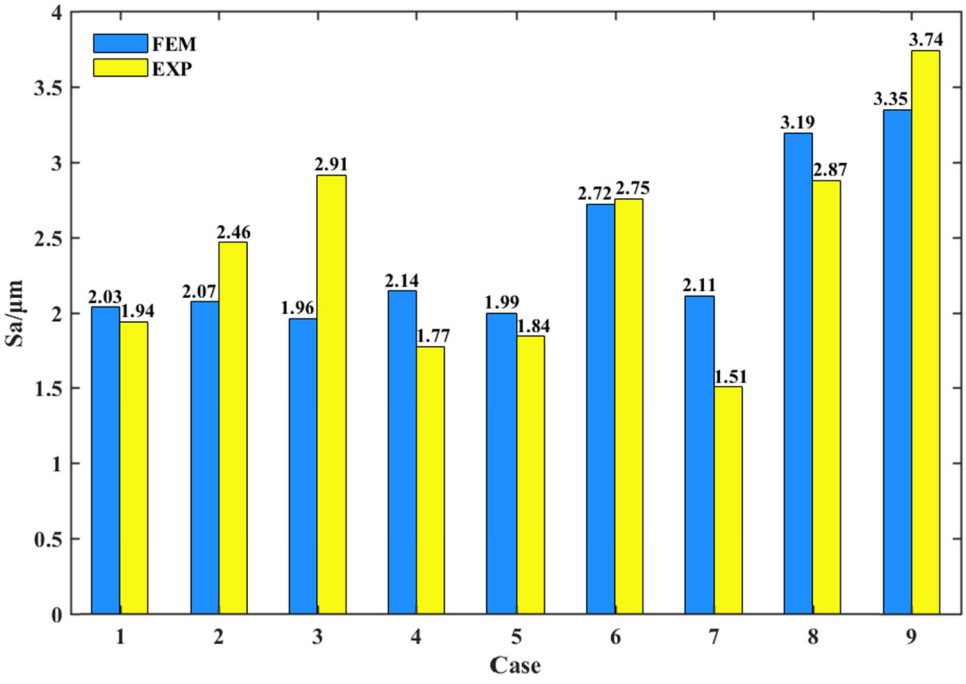

Figure 9: The comparison of S_a in Z direction between the test results and the corrected simulation model.

tool marks on the specimen surface, resulting in a certain roughness of the specimen surface before SP. However, the initial roughness of the target surface is not considered in the simulation model, so the results obtained by FEA need to be corrected. The correction formula is as follows:

$$S_a' = k \cdot S_a + b, \tag{7}$$

where S_a is the roughness of the simulation model before correction, S_a' is the roughness of the simulation model after correction, k is the influence coefficient of the shot set as the rigid body on the roughness, and b is the influence constant of the initial roughness on the roughness after SP.

The node displacements of four groups in simulation models with the same process parameters are extracted to calculate the roughness, and the average value of four groups of models is obtained. Then, the mean value is taken as the roughness of the simulation model before correction and linearly fitted with the experimental value by the least square method. Thus, $k = 0.17$, $b = 1.5$, and Eq. (7) can be expressed as:

$$S_a' = 0.17 \cdot S_a + 1.5. \tag{8}$$

Table A4 shows the solution results of S_a by the simulation model, and Figure 9 shows the comparison between the measured and the corrected simulated results. The average relative error of S_a between the simulation and the experiment is 16.14%.

Experimental results show that Case 7 has the lowest roughness of 1.51 μm among all shot-peened specimens, and Case 9 has the highest roughness of 3.74 μm. The average value of S_a measured results are analyzed by range method, and the range analysis results are shown in Table 8.

Table 8: Results of range analysis of S_a

Factor	*A* – shot diameter	*B* – impact velocity	*C* – impact angle
Average of level 1	2.44 ± 0.49	1.74 ± 0.22	2.52 ± 0.51
Average of level 2	2.12 ± 0.55	2.39 ± 0.52	2.66 ± 1.00
Average of level 3	2.71 ± 1.13	3.13 ± 0.53	2.08 ± 0.73
Range	0.58	1.40	0.57
Factor primary → secondary	*BAC*		
Optimal plan		$A_2B_1C_3$	

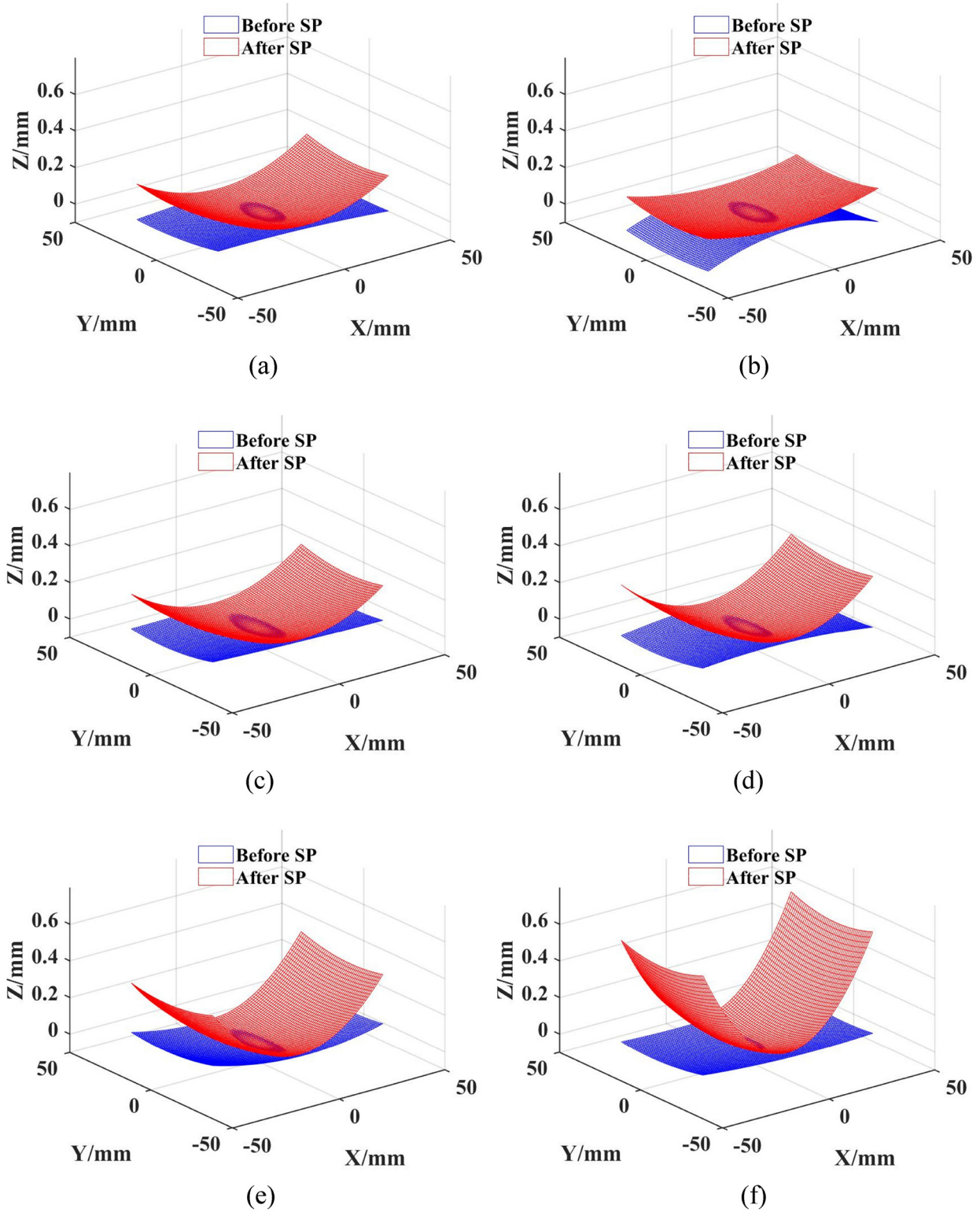

Figure 10: The comparison of deformation results of bottom surface of specimen before and after SP. (a) Case 1 (0.2 mm/60 m·s^{-1}/90°). (b) Case 2 (0.2 mm/80 m·s^{-1}/60°). (c) Case 3 (0.2 mm/100 m·s^{-1}/30°). (d) Case 4 (0.3 mm/60 m·s^{-1}/60°). (e) Case 5 (0.3 mm/80 m·s^{-1}/30°). (f) Case 6 (0.3 mm/100 m·s^{-1}/90°). (g) Case 7 (0.5 mm/60 m·s^{-1}/30°). (h) Case 8 (0.5 mm/80 m·s^{-1}/90°). (i) Case 9 (0.5 mm/100 m·s^{-1}/60°).

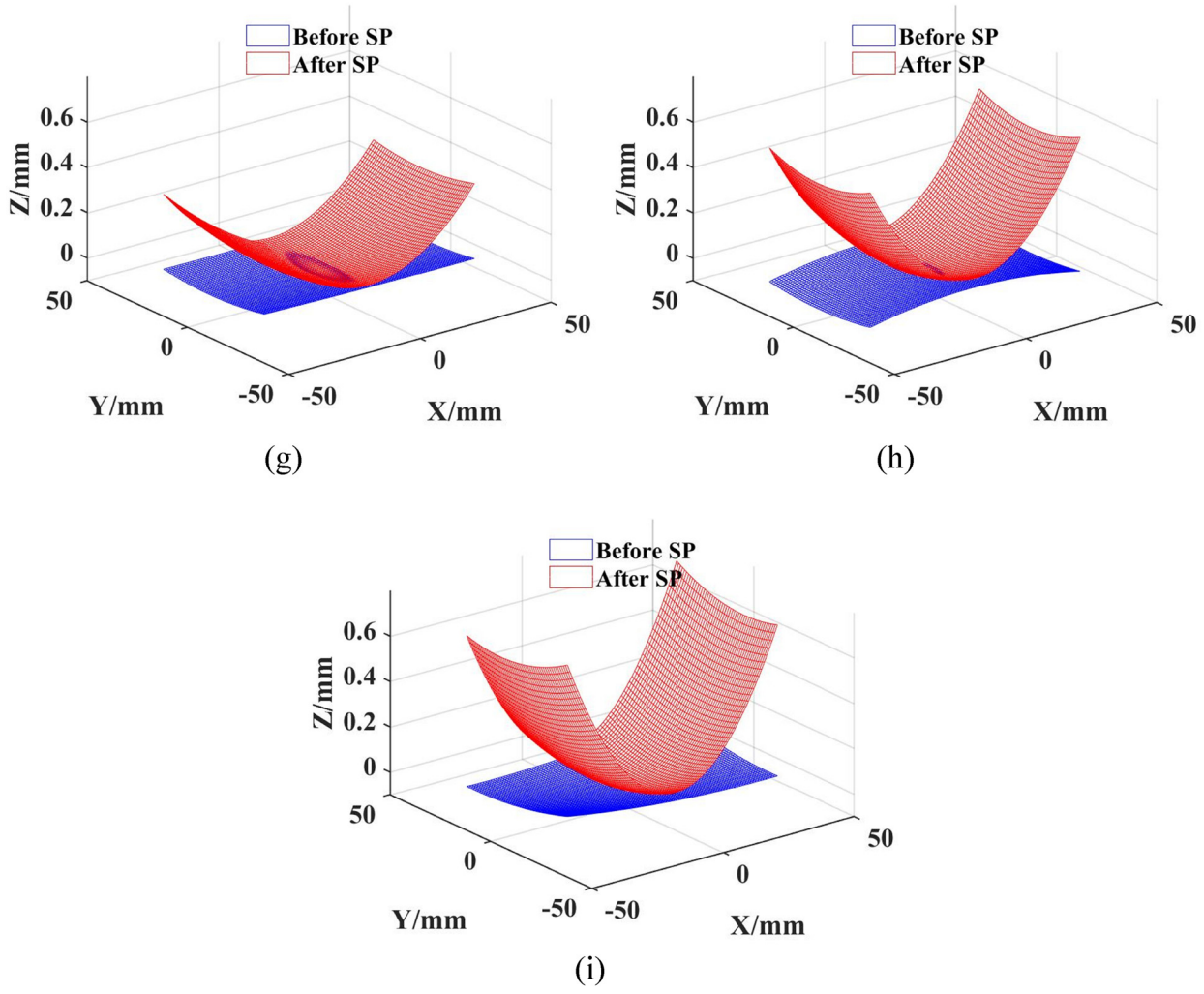

Figure 10: (*Continued*)

According to Table 8, it can be seen that the extreme difference of factor B is the largest and is much larger than the other two factors, which indicates that the level of factor B has the greatest influence on the experimental results and it is the most important factor affecting S_a of SP. The extreme difference between factor A and C is very close, which indicates that these two factors have a similar effect on S_a. Factors sorted by influence weight from large to small are B (impact velocity), A (shot diameter), and C (impact angle). The best process combination for S_a is $A_2B_1C_3$, that is, shot diameter of 0.3 mm, shot speed of 60 m·s^{-1}, and impact angle of 30°. S_a caused by 0.3 mm shot is smaller than that caused by 0.2 mm shot, because the crater diameter of 0.3 mm shot is larger and the number of shots required in the same area is smaller when the coverage rate is 98%. Therefore, the crater density of the shot with diameter of 0.3 mm is smaller than that of 0.2 mm. Hence, the roughness is smaller.

3.3 Deformation of specimens

The measured deformations of P1–P20 before and after SP are fitted by quadratic polynomial fitting with least squares method, respectively, and Table A5 shows the fitting errors. Sum of squares for error (SSE) refers to the square of error between fitting data and corresponding points of original data. The fitting accuracy is the highest when SSE is 0, and it decreases with the increase in SSE. R-square (determination coefficient) represents the fitting quality by the change in data and the range of R-square is [0, 1]. The closer R-square is to 1, the stronger the explanatory ability of variables of equation to Z value is, and the better the fitting effect is.

Table A5 shows that the SSE of specimen surface fitting before and after SP is basically less than 1×10^{-3}, and most of the R-square values are greater than 0.99, which shows that it is reasonable to select the second order polynomial to fit the measuring point.

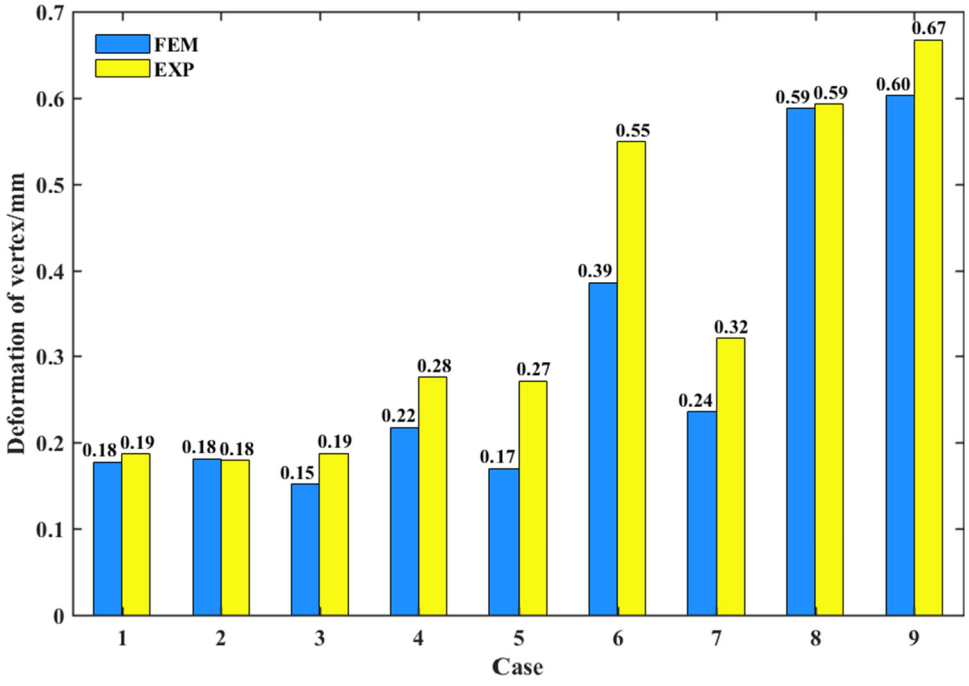

Figure 11: The comparison of vertex deformation in Z direction between simulation and experiment.

During the deformation measurement tests, the shot-peened surface of the specimen is fixed by plasticene, but the height of each specimen padded with plasticene and the inclination angle between the specimen and the workbench are not consistent. Therefore, MATLAB is used to translate and rotate the fitted surface so that the value at the center point P0 of each specimen measuring surface is 0 and the normal direction of the surface at point P0 is parallel to the Z axis.

Figure 10 is the comparison of deformation results before and after SP of Cases 1–9. The average value after SP minus the value before SP is the deformation of the bottom surface vertex caused by SP. Table A6 shows the deformation of specimen in simulation model, and Figure 11 shows the deformation comparison between simulation and experiment.

Figure 11 shows that the simulated deformations are very close to the experiment. The average relative error of deformation value is 16.73%, which validates the accuracy of the simulation model. The deformations of Case 6, Case 8, and Case 9 are relatively large, and the deformation of each specimen in X direction is significantly greater than that in Y direction because of the stiffener structure in Y direction. As presented in Table 9, the range value of each factor is obtained by range analysis based on the measured deformations.

According to Table 9, it can be seen that the extreme difference of factor A is the largest, which indicates that the level of factor A has the greatest influence on the measured results and is the most important factor affecting the deformation of SP. The extreme difference between factor B and C is very close, which indicates that the level of these two

Table 9: Range analysis results of deformation

Factor	A – shot diameter	B – impact velocity	C – impact angle
Average of level 1	0.18 ± 0.00	0.26 ± 0.07	0.44 ± 0.22
Average of level 2	0.37 ± 0.16	0.35 ± 0.22	0.37 ± 0.26
Average of level 3	0.53 ± 0.18	0.47 ± 0.25	0.26 ± 0.07
Range	0.3422	0.2068	0.1828
Factor primary → secondary	ABC		
Optimal plan		$A_1B_1C_3$	

factors has a similar effect on the deformation of specimen. The influence weight of each factor from large to small is: *A* (shot diameter), B (impact velocity), and *C* (impact angle). The best process combination for deformation is $A_1B_1C_3$. That is, shot diameter of 0.2 mm, shot speed of 60 m·s^{-1}, and impact angle of 30°. It demonstrated that the velocity of the projectile perpendicular to the peening surface decreases with the shot diameter, which also causes the decrease in the impact energy and resulting deformation.

4 Conclusion

In this study, a random multiple impingement SP simulation model is established to explore the effect of SP process parameters on the residual stress, surface integrity, and deformation. The corresponding experiments are conducted to validate the proposed model. The optimal process parameters, including shot diameter, impact velocity, and impact angle, are analyzed and conclusions are drawn as follows:

1) Random multiple impingement SP simulation model has different calculation results due to different number of shots. The randomness of simulation results can be reduced to a certain extent by generating random coordinates of shot several times and modeling by taking the average number of shots. And the relationship between average number of shots N, shot diameter D_1, crater diameter D_2 is: $N = 217.3 \cdot \frac{D_1}{D_2} - 313.5$.
2) The shot diameter is the most important factor affecting the stress hardening effect of SP. The order of each factor from primary to secondary is: shot diameter, impact angle, and impact velocity. The optimal process combination for stress strengthening is shot diameter of 0.5 mm, shot speed of 100 m·s^{-1}, and impact angle of 90°.
3) The impact velocity is the most important factor affecting roughness. The order of each factor from primary to secondary is: impact velocity, shot diameter, and impact angle. The best process combination for surface roughness is shot diameter of 0.3 mm, shot speed of 60 m·s^{-1}, and impact angle of 30°.
4) The shot diameter is the most important factor affecting the deformation of SP. The order of each factor from primary to secondary is: shot diameter, impact velocity, and impact angle. The best process combination for deformation is shot diameter of 0.2 mm, shot speed of 60 m·s^{-1}, and impact angle of 30°.

Acknowledgements: The authors thank Xinrui Tao for revising the manuscript.

Author contributions: Hanjun Gao: conceptualization, methodology, writing – original draft, and funding acquisition; Minghui Lin: investigation, conceptualization, validation, and writing – original draft; Jing Guo: validation and writing – review and editing; Liang Yang: formal analysis and visualization; Qiong Wu: resources, supervision, data curation, and funding acquisition; Ziliang Ran: visualization; Nianpu Xue: visualization. All authors have accepted responsibility for the entire content of this manuscript and approved its submission.

Conflict of interest: The authors state no conflict of interest.

Data availability statement: The datasets generated during and/or analyzed during the current study are available from the corresponding author on reasonable request.

References

[1] Li, B. H., S. F. Wu, and X. S. Gao. Theoretical calculation of a TiO_2-based photocatalyst in the field of water splitting: A review. *Nanotechnology Reviews*, Vol. 9, 2020, pp. 1080–1103.
[2] Song, H. C., H. J. Gao, Q. Wu, and Y. D. Zhang. Residual stress relief mechanisms of 2219 Al-Cu alloy by thermal stress relief method. *Reviews on Advanced Materials Science*, Vol. 61, 2022, pp. 102–116.
[3] Gao, H. J., Y. D. Zhang, Q. Wu, and B. H. Li. Investigation on influences of initial residual stress on thin-walled part machining deformation based on a semi-analytical model. *Journal of Materials Processing Technology*, Vol. 262, 2018, pp. 437–448.
[4] Li, B. H., H. B. Deng, H. David, and Z. Hu. A semi-analytical model for predicting the machining deformation of thin-walled parts considering machining-induced and blank initial residual stress. *The International Journal of Advanced Manufacturing Technology*, Vol. 110, 2020, pp. 1–23.
[5] Gao, H. J., S. F. Wu, Q. Wu, B. H. Li, Z. H. Gao, Y. D. Zhang, et al. Experimental and simulation investigation on thermal-vibratory stress relief process for 7075 aluminium alloy. *Materials & Design*, Vol. 195, 2020, pp. 1–14.
[6] Sun, H. L., X. X. Lian, X. X. Huang, H. David, and G. X. Wang. Effects of substrate properties and sputtering methods on self-formation of Ag particles on the Ag–Mo (Zr) alloy films. *Nanotechnology Reviews*, Vol. 9, 2020, pp. 990–997.
[7] Ni, H. T., L. X. Wang, Z. D. Wang, and J. Zhu. Grain orientation induced softening in electrodeposited gradient nanostructured nickel during cold rolling deformation. *Reviews on Advanced Materials Science*, Vol. 59, 2020, pp. 144–150.
[8] Li, S. N., D. Du, L. Zhang, X. G. Song, Y. G. Zheng, G. Q. Huang, et al. A review on filler materials for brazing of carbon-carbon

composites. *Reviews on Advanced Materials Science*, Vol. 60, 2021, pp. 92–111.
[9] Zhao, Y. H. and Y. L. Gu. Deformation mechanisms and plasticity of ultrafine-grained Al under complex stress state revealed by digital image correlation technique. *Nanotechnology Reviews*, Vol. 10, 2021, pp. 73–86.
[10] Gao, Z. H., H. J. Gao, Y. D. Zhang, Q. Wu, S. G. Chen, and X. Zhou. Study on stress distribution of SiC/Al composites based on microstructure models with microns and nanoparticles. *Nanotechnology Reviews*, Vol. 11, 2022, pp. 1854–1869.
[11] Jiang, Q., S. S. Tallury, Y. P. Qiu, and M. A. Pasquinelli. Interfacial characteristics of a carbon nanotube-polyimide nanocomposite by molecular dynamics simulation. *Nanotechnology Reviews*, Vol. 9, 2020, pp. 136–145.
[12] Wang, J. L., Y. B. Zhang, X. Yang, and X. B. Ma. Stress effect on 3D culturing of MC3T3-E1 cells on microporous bovine bone slices. *Nanotechnology Reviews*, Vol. 9, 2020, pp. 1315–1325.
[13] Zhang, J. R., F. Yang, Y. P. Liu, Z. Zhong, and J. F. Zhao. On the deformation-induced grain rotations in gradient nano-grained copper based on molecular dynamics simulations. *Nanotechnology Reviews*, Vol. 10, 2021, pp. 87–98.
[14] Akbar, M. and B. Mehmood. Global experience of HVDC composite insulators in outdoor and indoor environment. *Reviews on Advanced Materials Science*, Vol. 59, 2020, pp. 606–618.
[15] Khun, N. W., P. Q. Trung, and D. L. Butler. Mechanical and tribological properties of shot-peened SAE 1070 steel. *Tribology Transactions*, Vol. 59, 2016, pp. 932–943.
[16] Zhan, K., C. H. Jiang, and V. Ji. Uniformity of residual stress distribution on the surface of S30432 austenitic stainless steel by different shot peening processes. *Materials Letters*, Vol. 99, 2013, pp. 61–64.
[17] Wang, C. Y., W. G. Li, J. J. Jiang, X. Chao, W. K. Zeng, and J. Yang. Mechanical behavior study of asymmetric deformation in double-sided symmetrical sequential shot peening process. *The International Journal of Advanced Manufacturing Technology*, Vol. 114, 2021, pp. 1189–1204.
[18] Zhang, X. J., T. Wang, J. B. Wang, and C. Liu. Analytical modeling of shot peen forming process using cross-sectional linear indentation coverage method. *International Journal of Mechanical Sciences*, Vol. 133, 2017, pp. 838–845.
[19] Gao, Y. K. Influence of shot peening on fatigue property of Ti-60 high temperature titanium alloy. *Surface Engineering*, Vol. 23, 2017, pp. 431–433.
[20] Mahmoudi, A. H., A. Ghasemi, G. H. Farrahi, and K. Sherafatnia. A comprehensive experimental and numerical study on redistribution of residual stresses by shot peening. *Materials & Design*, Vol. 90, 2016, pp. 478–487.
[21] Sherafatnia, K., G. H. Farrahi, and A. H. Mahmoudi. Effect of initial surface treatment on shot peening residual stress field: Analytical approach with experimental verification. *International Journal of Mechanical Sciences*, Vol. 137, 2018, pp. 171–181.
[22] Marini, M., F. Piona, V. Fontanari, M. Bandini and M. Benedetti. A new challenge in the DEM/FEM simulation of the shot peening process: The residual stress field at a sharp edge. *International Journal of Mechanical Sciences*, Vol. 169, 2019, pp. 1–14.
[23] Ghasemi, A., S. M. Hassani-Gangaraj, A. H. Mahmoudi, and G. H. Farrahi. Shot peening coverage effect on residual stress profile by FE random impact analysis. *Surface Engineering*, Vol. 32, 2016, pp. 861–870.
[24] Atig, A., R. B. Sghaier, R. Seddik, and R. Fathallah. Probabilistic methodology for predicting the dispersion of residual stresses and Almen intensity considering shot peening process uncertainties. *International Journal of Advanced Manufacturing Technology*, Vol. 94, 2017, pp. 2125–2136.
[25] Tan, L., D. H. Zhang, C. F. Yao, D. X. Wu, and J. Y. Zhang. Evolution and empirical modeling of compressive residual stress profile after milling, polishing and shot peening for TC17 alloy. *Journal of Manufacturing Processes*, Vol. 26, 2017, pp. 155–165.
[26] Zhu, K. Y., C. H. Jiang, Z. Q. Li, L. B. Du, Y. T. Zhao, Z. Chai, et al. Residual stress and microstructure of the CNT/6061 composite after shot peening. *Materials & Design*, Vol. 107, 2016, pp. 333–340.
[27] Chen, M., H. B. Liu, L. B. Wang, C. X. Wang, K. Y. Zhu, Z. Xu, et al. Evaluation of the residual stress and microstructure character in SAF 2507 duplex stainless steel after multiple shot peening process. *Surface & Coatings Technology*, Vol. 344, 2018, pp. 132–140.
[28] Trsko, L., O. Bokuvka, F. Novy, and M. Guagliano. Effect of severe shot peening on ultra-high-cycle fatigue of a low-alloy steel. *Materials & Design*, Vol. 57, 2014, pp. 103–113.
[29] Vazquez, J., C. Navarro, and J. Dominguez. Experimental results in fretting fatigue with shot and laser peened Al 7075-T651 specimens. *International Journal of Fatigue*, Vol. 40, 2012, pp. 143–153.
[30] Wu, Q., D. J. Xie, Z. M. Jia, Y. D. Zhang, and H. Z. Zhang. Effect of shot peening on surface residual stress distribution of SiCp/2024Al. *Composites Part B Engineering*, Vol. 154, 2018, pp. 382–387.
[31] Bagherifard, S., I. Fernandez-Pariente, R. Ghelichi, and M. Guagliano. Effect of severe shot peening on microstructure and fatigue strength of cast iron. *International Journal of Fatigue*, Vol. 65, 2014, pp. 64–70.
[32] Bagherifard, S., S. Slawik, I. Fernández-Pariente, C. Pauly, F. Muecklich, and M. Guagliano. Nanoscale surface modification of AISI 316L stainless steel by severe shot peening. *Materials & Design*, Vol. 102, 2016, pp. 68–77.
[33] Hassani-Gangaraj, S. M., K. S. Cho, H. J. L. Voigt, M. Guagliano, and C. A. Schuh. Experimental assessment and simulation of surface nanocrystallization by severe shot peening. *Acta Materialia*, Vol. 97, 2015, pp. 105–115.
[34] Almangour, B. and J. M. Yang. Improving the surface quality and mechanical properties by shot-peening of 17-4 stainless steel fabricated by additive manufacturing. *Materials & Design*, Vol. 110, 2016, pp. 914–924.
[35] Sun, R. J., L. H. Li, Y. Zhu, W. Guo, P. Peng, B. Q. Cong, et al. Microstructure, residual stress and tensile properties control of wire-arc additive manufactured 2319 aluminum alloy with laser shock peening. *Journal of Alloys & Compounds*, Vol. 747, 2018, pp. 255–265.
[36] Sorsa, A., S. Santa-Aho, J. Wartiainen, L. Suominen, M. Vippola, and K. Leiviska. Effect of shot peening parameters to residual stress profiles and Barkhausen noise. *Journal of Nondestructive Evaluation*, Vol. 37, 2018, pp. 1–11.
[37] Gujba, A. K. and M. Medraj. Laser peening process and its impact on materials properties in comparison with shot peening and ultrasonic impact peening. *Materials*, Vol. 7, 2014, pp. 7925–7974.
[38] Lu, S. N. and N. He. Dynamic constitutive model of TC4 alloy material and finite element simulation of orthogonal high-

speed cutting. *Weapons Materials Science and Engineering*, Vol. 32, 2009, pp. 5–9.
[39] Don, L. *Experimental investigation of material models for Ti6Al4V and 202-T3 aluminum: DOT/FAA/AR-00/25* [*R*], FAA, Washington, D. C., 2000.
[40] Wang, Y. Z., F. Li, Y. Y. Chen, Y. P. Zhang, Z. G. Wu, and C. Wang. TC4 shot peening simulation and experiment. *Journal of BeiHang University*, Vol. 45, 2019, pp. 1723–1731.
[41] Wu, S. J., H. J. Liu, R. H. Zhang, X. H. Zhang, and Y. B. Ge. Parameter prediction of shot peening surface integrity based on orthogonal experiments and data driven. *Surface Technology*, Vol. 50, 2021, pp. 86–95.
[42] Chen, J. W., K. Liao, L. J. Li, Z. C. Gao, and L. P. Zhong. Simulation analysis and experiment of the effect of different shot particles on aluminum alloy surface peening. *Surface Technology*, Vol. 48, 2019, pp. 121–126.

Appendix

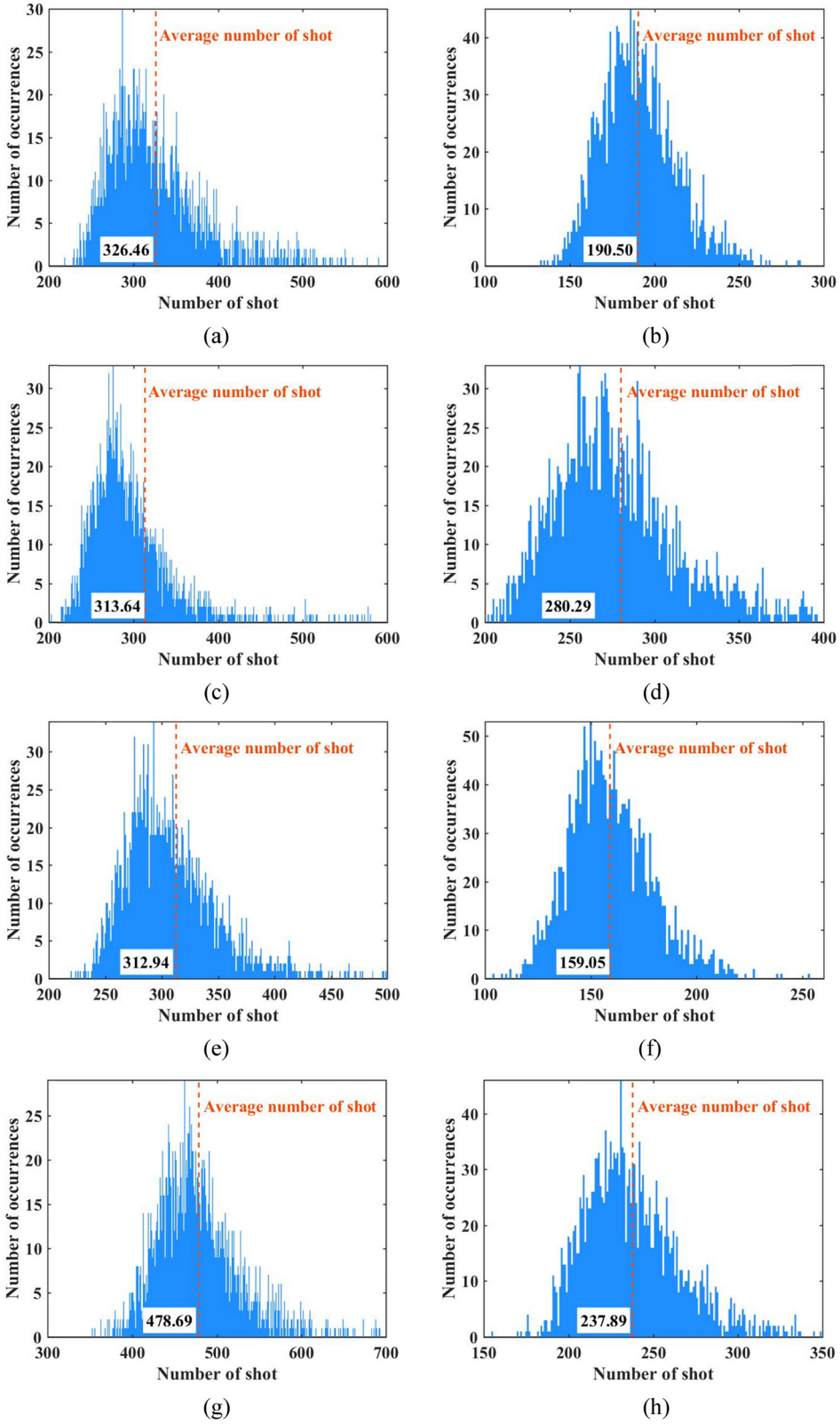

Figure A1: 2,000 times calculation of shot number distribution. (a) Case 1 (0.2 mm/60 m·s^{-1}/90°). (b) Case 2 (0.2 mm/80 m·s^{-1}/60°). (c) Case 3 (0.2 mm/100 m·s^{-1}/30°). (d) Case 4 (0.3 mm/60 m·s^{-1}/60°). (e) Case 5 (0.3 mm/80 m·s^{-1}/30°). (f) Case 6 (0.3 mm/100 m·s^{-1}/90°). (g) Case 7 (0.5 mm/60 m·s^{-1}/30°). (h) Case 8 (0.5 mm/80 m·s^{-1}/90°).

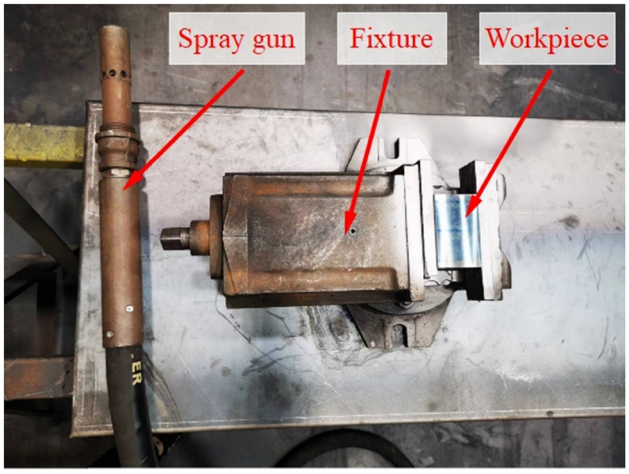

Figure A2: SP site.

Table A1: Injection pressure corresponding to orthogonal experimental process plan

Case	Shot diameter (mm)	Shot velocity ($m \cdot s^{-1}$)	Incident angle (°)	SP pressure (bar)
1	0.2	60	90	1.7
2	0.2	80	60	3.6
3	0.2	100	30	5.8
4	0.3	60	60	1.8
5	0.3	80	30	3.7
6	0.3	100	90	5.8
7	0.5	60	30	2.0
8	0.5	80	90	3.8
9	0.5	100	60	5.9

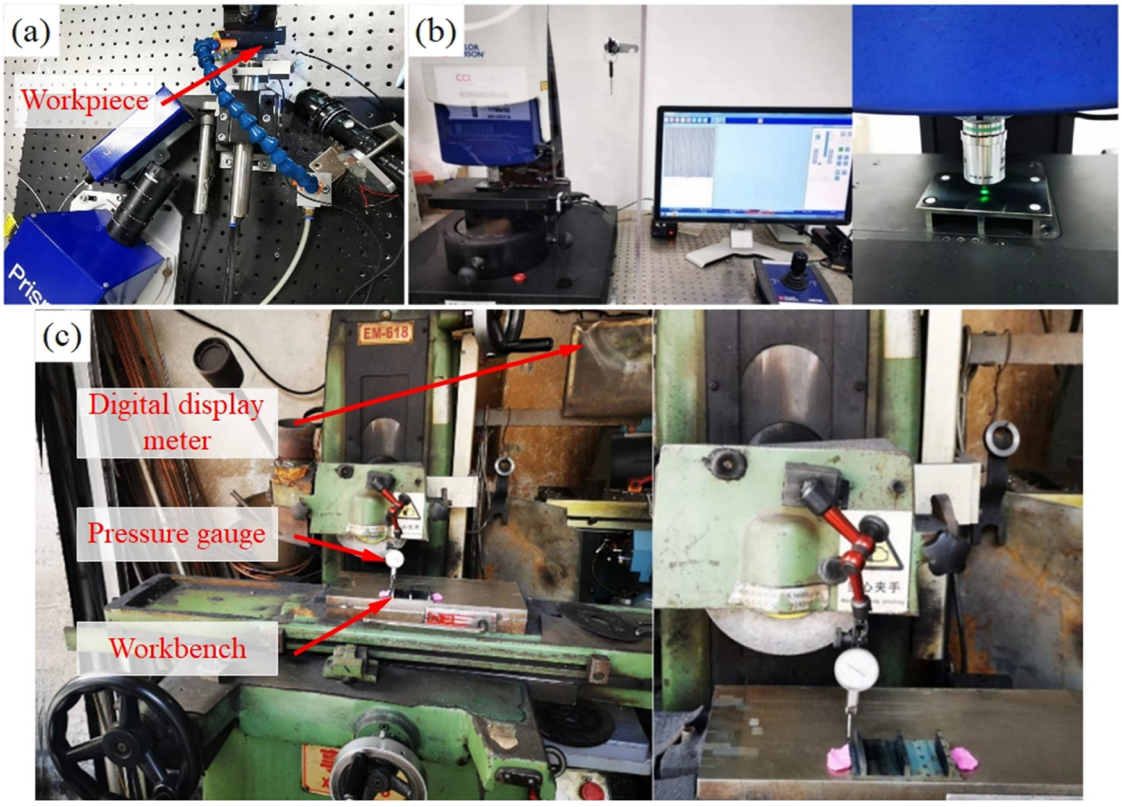

Figure A3: Experimental test. (a) Residual stress test; (b) Roughness test; (c) Deformation test.

Table A2: Maximum residual compressive stress of simulation and experiment

Case	FEM(MPa)			EXP(MPa)			Relative error (%)
	X	*Y*	Average	*X*	*Y*	Average	
1	−822.10	−819.69	−820.89	−628	−947	−787.5	4.24
2	−782.69	−793.62	−788.15	−557	−643	−600.0	31.36
3	−778.25	−814.40	−796.33	−382	−405	−393.5	102.37
4	−780.15	−792.33	−786.24	−605	−608	−606.5	29.64
5	−766.33	−822.59	−794.46	−592	−778	−685.0	15.98
6	−796.94	−787.18	−792.06	−609	−704	−656.5	20.65
7	−821.26	−864.87	−843.06	−546	−748	−647.0	30.30
8	−813.41	−815.71	−814.56	−662	−594	−628.0	29.71
9	−780.51	−789.59	−785.05	−690	−679	−684.5	14.69

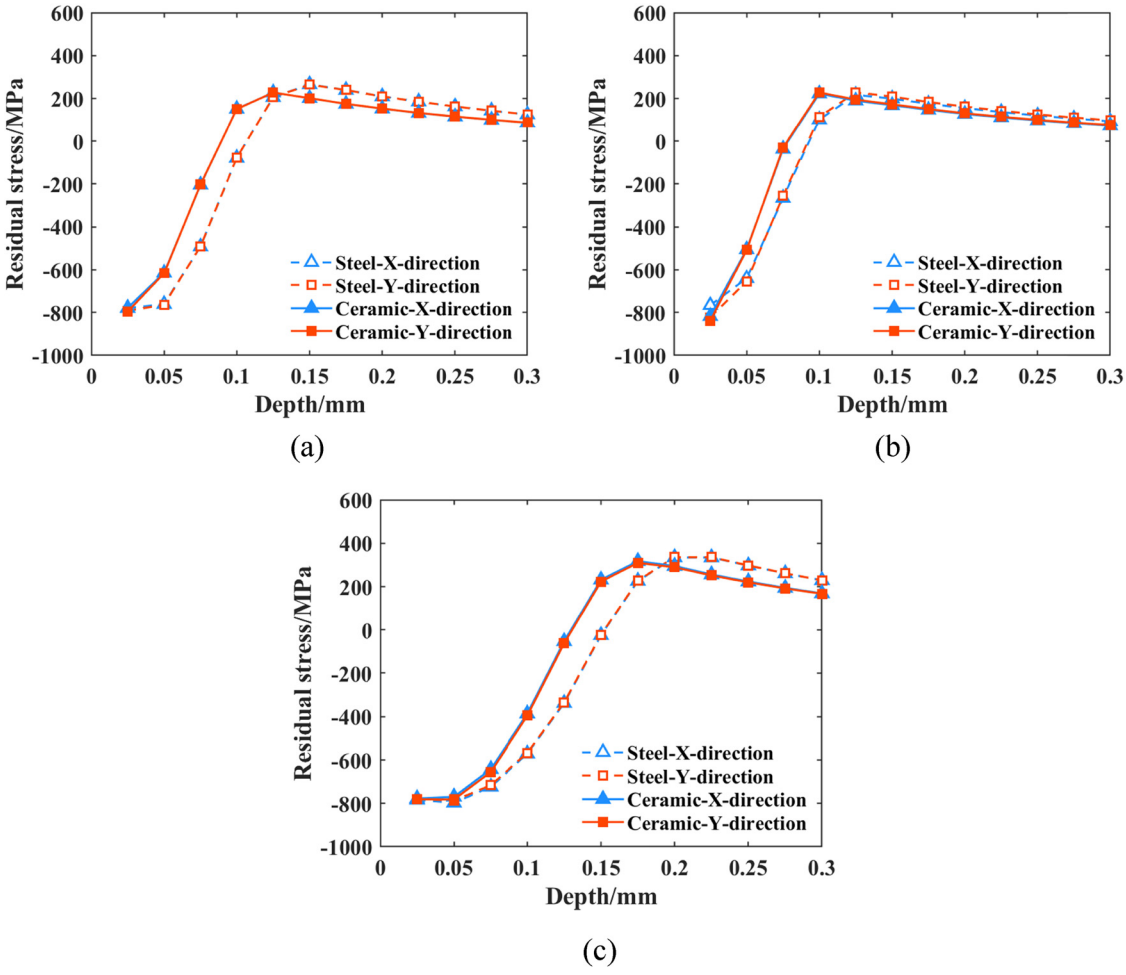

Figure A4: The comparison results of steel shot SP and ceramic shot SP. (a) Case 4-steel and Case 4- ceramic (0.3 mm/60 m·s^{-1}/60°). (b) Case 5-steel and Case 5-ceramic (0.3 mm/80 m·s^{-1}/30°). (c) Case 6-steel and Case 6-ceramic (0.5 mm/100 m·s^{-1}/60°).

Table A3: Test results of S_a

Case	P1	P2	P3	Average
1	1.9012	1.9156	1.9938	1.9369
2	2.5907	2.3497	2.4483	2.4629
3	2.8580	3.1324	2.7393	2.9099
4	1.8365	1.7060	1.7776	1.7734
5	1.9663	1.9861	1.5653	1.8392
6	2.9558	2.7059	2.6000	2.7539
7	1.4711	1.5435	1.5004	1.5050
8	2.5430	3.0531	3.0244	2.8735
9	3.8446	3.6213	3.7551	3.7403
10	1.3569	1.2090	1.2931	1.2863

Table A5: Fitting effect of workpiece surface

Case	Before SP		After SP	
	SSE	*R*-square	SSE	*R*-square
1	0.0020	0.9354	8.96×10^{-4}	0.9913
2	1.58×10^{-4}	0.9961	5.68×10^{-4}	0.9756
3	3.11×10^{-4}	0.9944	3.13×10^{-4}	0.9974
4	5.82×10^{-4}	0.89894	3.42×10^{-4}	0.9984
5	5.24×10^{-4}	0.9937	1.96×10^{-4}	0.9995
6	1.82×10^{-4}	0.9957	4.63×10^{-4}	0.9996
7	5.63×10^{-4}	0.8875	3.38×10^{-4}	0.9991
8	1.30×10^{-4}	0.9910	0.0012	0.9987
9	2.07×10^{-4}	0.9907	0.0019	0.9988
10	2.53×10^{-4}	0.9914	2.53×10^{-4}	0.9914

Table A4: S_a of the simulation model

Case	Model 1	Model 2	Model 3	Model 4	Average	After correction	Error with experimental value (%)
1	3.0071	3.1563	3.1227	3.2559	3.1355	2.0330	4.97
2	3.2179	3.4297	3.3846	3.3464	3.3447	2.0686	−16.01
3	2.6458	2.8023	2.7210	2.6694	2.7096	1.9606	−32.62
4	3.6577	3.8081	3.6620	3.9285	3.7641	2.1399	20.67
5	2.9942	2.8212	3.0787	2.6829	2.8942	1.9920	8.31
6	7.0777	7.1780	7.0521	7.3587	7.1666	2.7183	−1.29
7	3.5069	3.7255	3.6074	3.4314	3.5678	2.1065	39.97
8	10.3243	9.0319	10.6701	9.6517	9.9195	3.1863	10.89
9	11.3989	10.8524	10.4644	10.7285	10.8611	3.3464	−10.53

Table A6: Deformation of workpiece in simulation model

Case	Model 1	Model 2	Model 3	Model 4	Average	Error with experimental value (%)
1	0.1745	0.1850	0.1716	0.1802	0.1778	−4.85
2	0.1782	0.1811	0.1838	0.1830	0.1815	1.22
3	0.1500	0.1511	0.1538	0.1519	0.1517	−19.16
4	0.2177	0.2161	0.2141	0.2231	0.2178	−21.07
5	0.1708	0.1664	0.1688	0.1732	0.1698	−37.47
6	0.3913	0.3583	0.3943	0.3968	0.3852	−29.82
7	0.2347	0.2368	0.2354	0.2355	0.2356	−26.53
8	0.5879	0.5879	0.5837	0.5915	0.5877	−0.79
9	0.5951	0.6098	0.5911	0.6150	0.6028	−9.67